Streaming from the Equator of a Drop in an External Electric Field

Quentin Brosseau and Petia M. Vlahovska*
School of Engineering, Brown University, Providence, Rhode Island 02912, USA
(Received 16 January 2017; revised manuscript received 9 May 2017; published 20 July 2017)

Tip streaming generates micron- and submicron-sized droplets when a thin thread pulled from the pointy end of a drop disintegrates. Here, we report streaming from the equator of a drop placed in a uniform electric field. The instability generates concentric fluid rings encircling the drop, which break up to form an array of microdroplets in the equatorial plane. We show that the streaming results from an interfacial instability at the stagnation line of the electrohydrodynamic flow, which creates a sharp edge. The flow draws from the equator a thin sheet which destabilizes and sheds fluid cylinders. This streaming phenomenon provides a new route for generating monodisperse microemulsions.

DOI: 10.1103/PhysRevLett.119.034501

A drop in a uniform electric field can form conical tips at the poles (Taylor cones) emitting jets of charged tiny droplets [1–4]. This so-called electrohydrodynamic (EHD) tip streaming or cone jetting occurs in many natural phenomena (e.g., drops in thunderclouds) and technological applications (printing, electrospraying, electrospinning) [1,5].

The streaming is related to a generic interfacial instability due to a convergent flow [6]; see Fig. 1(a). The interface is compressed and a local perturbation at the stagnation point (e.g., drop tips) gets drawn by the flow. When the viscous stresses overcome the interfacial tension, the perturbation grows into a fluid filament. This is the tip streaming phenomenon commonly observed in the microfluidic coflow geometry [7–9]. If, instead of a point, the flow is converging to a stagnation line, a thin sheet can be entrained [10]. In analogy with the cone-jet geometry resulting from the destabilization of a stagnation point, it is expected that the instability of a stagnation line would give rise to an edge-sheet structure. In this Letter, we report streaming resulting from a stagnation line instability at the equator of a drop: EHD equatorial streaming, which creates "Saturn rings" around the drop [see Fig. 1(b)].

Experimentally, we exploit the electrohydrodynamic flow near a neutral drop placed in a uniform electric field [11,12]. By varying the fluid conductivities, we are able to create a flow converging either at the drop poles [Fig. 1(c)], to generate a cone jet, or at the equator [Fig. 1(d)], to generate an edge sheet. The latter case is the focus of this Letter.

The electrohydrodynamic flow is driven by electric shear stresses due to induced surface charges [11,12]. For a drop in a uniform electric field, the resulting flow is axisymmetrically aligned with the applied field. For a spherical drop with radius a placed in a dc electric field $\mathbf{E} = E\hat{\mathbf{z}}$, the surface velocity is [11]

$$\mathbf{u}_T = \frac{a\varepsilon_{ex}E^2}{\mu_{ex}} \frac{9(S-R)}{10(1+\lambda)(R+2)^2} \sin(2\theta)\hat{\boldsymbol{\theta}}, \qquad (1)$$

where $\lambda = \mu_{in}/\mu_{ex}$ is the viscosity ratio between the drop and suspending fluids and θ is the angle with the applied field direction. The direction of the surface flow depends on the difference between the conductivity, σ, and the permittivity, ε, of the drop and suspending fluids $R = \sigma_{in}/\sigma_{ex}$ and $S = \varepsilon_{in}/\varepsilon_{ex}$. For drops with $R/S > 1$, the surface flow is from the equator to the poles. Accordingly, the poles become stagnation points where streaming occurs at sufficiently strong fields; see Fig. 1(c). Since the tips are also the location of the maximum induced charge ($Q \sim \cos\theta$), the emitted drops carry away some of it and become charged.

If the drop is less conductive than the suspending medium, $R/S < 1$, the surface flow is from the pole to

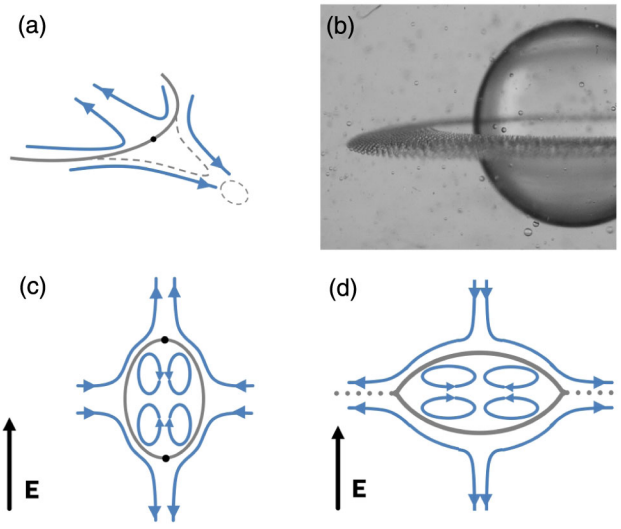

FIG. 1. (a) A protrusion at the stagnation point of a convergent flow can grow into a filament. (b) Rings of droplets formed via EHD streaming from the equator of a drop after application of a dc electric pulse. (c) For EHD flow near a drop with $R/S > 1$, the poles are stagnation points where cone jets form. (d) For EHD flow near a drop with $R/S < 1$, the equator is a stagnation line where an edge sheet is expected to form.

 © 2017 American Physical Society

the equator. Here, the equator is a stagnation line. Could streaming occur in such a geometry? What structures are formed? Surprisingly, drop stability under such conditions has been studied only to a very limited extent. Numerical studies [13–15] show that the drop either dimples at the poles to become a torus or flattens into a pancake shape. An experimental study also mentions a lenslike deformation [16]. Tiny drops are observed near the sharp edge, which hints at the possibility of a streaming instability. Intriguingly, flow convergence in a more complex geometry—a flattened droplet formed at the tip of a pendant drop and stretched by an electric field—can lead to rim ejection [17]. However, this instability is driven by charge concentration at an equatorial line, and the conductivity ratio is $R/S > 1$. Here, we show that streaming can occur even for $R/S < 1$ and in the absence of charge at the stagnation line. In this case, EHD equatorial streaming is characterized by the shedding of charge-free rings, which undergo capillary instability and break up into droplets.

Experiment.—The fluid system and experimental setup are similar to those used in Ref. [18]. Silicone oil (SO) and castor oil (CO) are used as drop and suspending fluids, respectively. Both fluids have low conductivity (on the order of 10^{-12} S/m) and high viscosity (100–1000 times that of water) (see Ref. [19] for detailed information). CO viscosity is $\mu_{ex} = 0.69$ Pa s, and SO viscosity is varied to adjust the viscosity ratio $\lambda = \mu_{in}/\mu_{ex}$ in the range between 0.001 and 10. For this system, the permittivity ratio is $S = \varepsilon_{in}/\varepsilon_{ex} = 0.6$ and the conductivity ratio $R = \sigma_{in}/\sigma_{ex} < S$. R is further lowered by doping the CO with the organic electrolyte TBAB (tetrabutylammonium bromide) or AOT (dioctyl sulfosuccinate sodium salt). The surface tension γ in all cases is measured to be 4.5 mN/m, confirming that the TBAB and AOT are not surface active in the SO-CO system. CO was changed for each experiment and the chamber thoroughly cleaned to avoid cross contamination. A uniform dc electric field is generated in a rectangular chamber built around two parallel ITO coated glass electrodes, both 75×50 mm and set 25 mm apart. In the experiment, a millimeter-sized drop is pipetted manually in the middle of the chamber, far from any boundary. Drop dynamics is recorded by CCD cameras placed either perpendicular to electric field or parallel to it. On the time scale of the experiment, drop sedimentation is negligible. Figure 2 illustrates the phenomenon of equatorial streaming.

Results.—The classic leaky-dielectric theory [11,12] predicts that, in weak electric fields, i.e., with electric capillary number $\mathrm{Ca} = \varepsilon_{ex} E^2 a/\gamma \ll 1$, a drop with $R/S < 1$ adopts an oblate spheroidal shape, the flow and shape being axisymmetrically aligned with the applied field. As the field strength increases, the drop undergoes various types of instabilities depending on the fluid viscosities and conductivities. Figure 3(a) maps the modes of droplet destabilization as a function of the fluid properties. There are three distinct modes: (A) Electrorotation ($R < S, \mathrm{Ca} > \mathrm{Ca}_Q$, any viscosity ratio λ). In this regime, the drop tilts relative to the applied

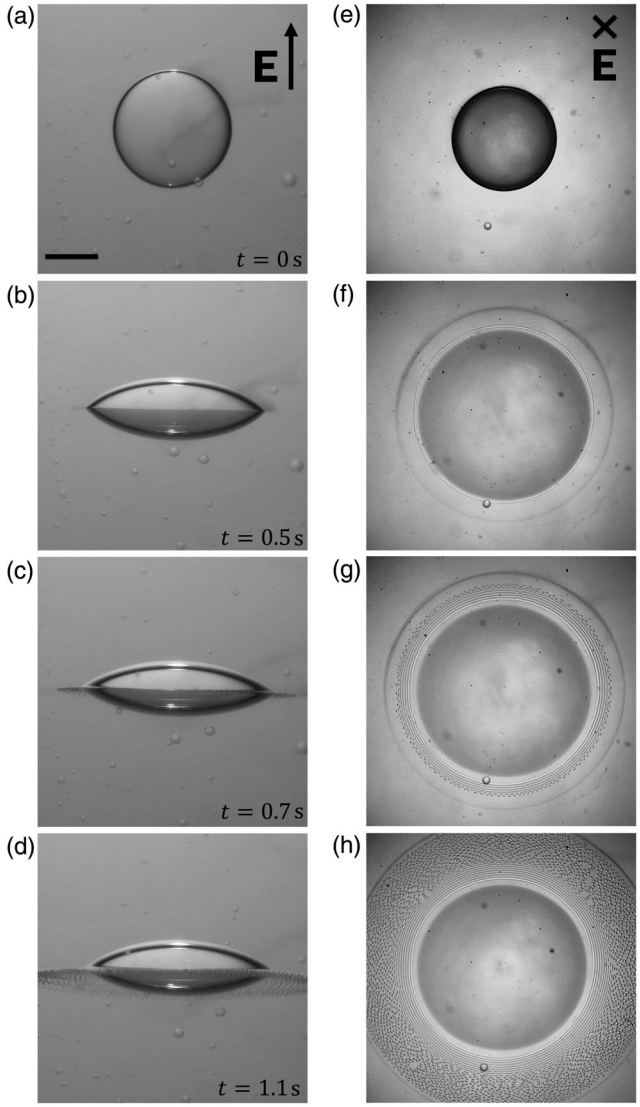

FIG. 2. EHD equatorial streaming observed from directions (a)–(d) perpendicular to and (e)–(h) perpendicular to the applied electric field; the field direction is the axis of symmetry. (a),(e) Spherical drops deform as the electric field is turned on at $t = 0$. (b)–(f) The mother drop flattens to an aspect ratio of about 0.5 and forms a lens with a sharp edge. (g),(h) The emission of rings occurs radially in the equatorial plane of the drop. The viscosity ratio is $\lambda = 0.07$. $E = 7.9$ kV/cm, $\mathrm{Ca} \sim 4$. The scale bar is 500 μm.

field direction; see Fig. 3(b). This symmetry breaking is due to the Quincke electrorotation [18,24–26], which gives rise to a rotational flow near the drop. The Quincke effect stabilizes the drop against breakup and even decreases interface deformation [27]. The threshold for electrorotation, E_Q, is estimated from the value for a rigid sphere [28],

$$E_Q^2 = \frac{2\sigma_{ex}\mu_{ex}(R+2)^2}{3\varepsilon_{ex}^2(S-R)}. \quad (2)$$

For the pure fluid system where $E_Q = 3$ kV/cm and for a typical drop with radius $a = 1$ mm, $\mathrm{Ca}_Q = 0.8$.

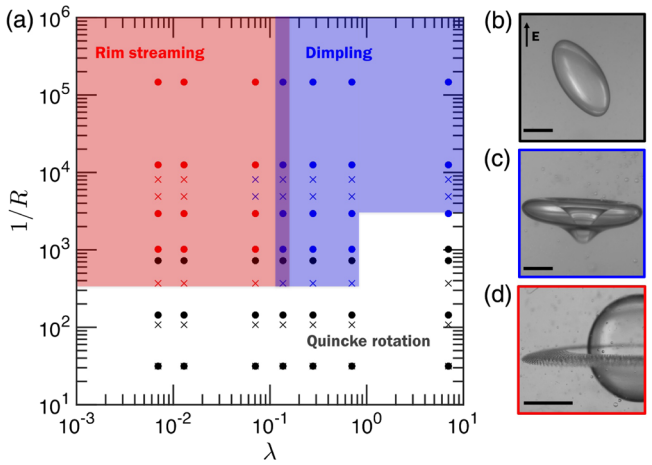

FIG. 3. Phase diagram of the drop dynamics in a strong, uniform dc electric field: Quincke electrorotation (black), dimpling (blue) for $\lambda > 0.1$, EHD equatorial streaming (red) for $\lambda < 0.1$. The conductivity of the suspending oil is modified by the addition of the electrolyte TBAB (the dots) or AOT (the crosses). $E \geq 3$ kV/cm. The scale bar is 500 μm. Images (b)–(d) illustrate the drop behaviors.

Adding electrolytes to the suspending fluid increases its conductivity, σ_{ex}, by several orders of magnitude and shifts the transition to Quincke to higher field strengths, thereby effectively suppressing the electrorotation. The critical conductivity ratio to suppress the electrorotation, R_c, is determined from Eq. (2) by solving for R_c, with $E = E_c$ being the desired Quincke threshold (e.g., for 1 MV/m, $R_c = 0.002$). Adding the dopant (TBAB or AOT) decreases R below the critical value. In the absence of electrorotation, $R < R_c$, the following two modes of drop fragmentation emerge. (B) Dimpling [$R \ll 1$, Ca $\sim O(1)$, $\lambda \geq 0.1$]. In this mode, the drop deforms into a biconcave disk with rounded rim and pinches in its center to form a torus [see Fig. 3(c)]; the torus subsequently breaks into a few drops [14,16,29]. The drop burst is abrupt and uncontrollable, and the resulting daughter-droplet size and number is irreproducible. This mode creates few drops with a size comparable to the mother drop. The critical capillary number is Ca $\sim O(1)$, corresponding to distorting electric stresses that can no longer be contained by the interfacial tension. The observed range of viscosity ratios, above $\lambda \sim O(1)$, for the dimpling is in agreement with numerical simulations [13,15]. (C) Equatorial streaming ($R \ll 1$, Ca ≥ 4, $\lambda \leq 0.1$). In this mode the drop flattens and forms a sharp edge with thin film attached to it (an edge sheet); see Fig. 2. The sheet emits concentric thin rings which break up into microdroplets; see Fig. 4. The ring shedding occurs in a steady manner, so droplet production can proceed for tens of seconds. Unlike dimpling, the streaming is a controllable process that is easily triggered and interrupted; e.g., see Fig. 1(b), which illustrates a mother drop surrounded by daughter droplets after the field is turned off. This streaming mode is able to produce thousands of microdroplets with a relatively uniform size distribution; see Fig. 5(a).

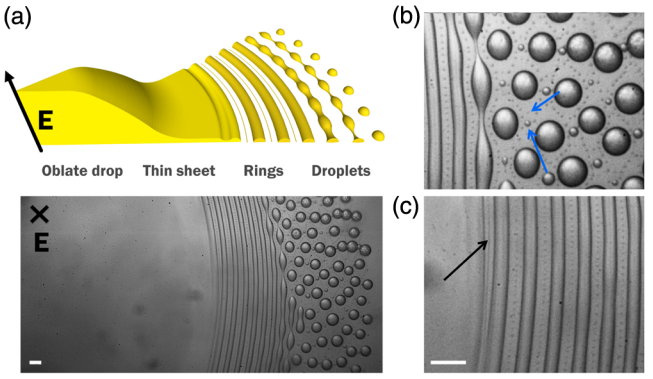

FIG. 4. EHD equatorial streaming. (a) 3D rendering of the phenomenon as deduced from the experiment ($\lambda = 0.07$) [19]. The thin sheet is visible as a slightly brighter region just prior to the edge where the ring is forming. A closer inspection reveals (b) two generations of satellite drops created after the ring breakup (the blue arrows) and (c) a satellite ring that breaks up in droplets (the black arrow). The scale bars are 100 μm.

The streaming morphology (sizes of rings and microdroplets, frequency of ring shedding) are insensitive to Ca and R in the explored range of parameters.

Mechanism of the EHD equatorial streaming.—The flow velocity at the onset of streaming is about 1 mm/s, which corresponds to Reynolds number $\rho_{ex} Ua/\mu_{ex} \sim 10^{-3}$. Hence, the EHD equatorial streaming is of a purely Stokesian nature, in contrast to the inertia dominated droplet splash and sheet disintegration [30–33]. Moreover, the interface polarization (charging) is much faster than the interface deformation due to the electrohydrodynamic flow [as seen by comparing the Maxwell-Wagner and electrohydrodynamic time scales: $t_{mw} = \varepsilon_{ex}(S+2)/\sigma_{ex}(R+2) \sim 1$ ms and $t_{ehd} = \mu_{ex}(1+\lambda)/\varepsilon_{ex}E^2 \sim 10$ ms]. Hence, the streaming in our system is controlled by the shear stresses [2,3], very much as in flow focusing, i.e., tip streaming induced by coflowing two fluids [34], and in contrast to the unsteady electrospray [35], where charge relaxation is non-negligible.

The phenomenon is a multistep process involving a downsizing cascade from one macrodrop to a thin edge sheet to concentric fluid rings to thousands of microdroplets; see Fig. 4.

At the onset of streaming, the drop forms a sharp edge at the equator from which a thin sheet extends. The critical capillary number can be estimated from linear stability analysis [6], which predicts that the cutoff instability wave number k^*a depends on the field strength, as $k^*a = 0.55$ Ca for our system [19]. For the instability to occur, the shortest unstable wavelength has to be smaller than the natural cutoff length (the drop perimeter), i.e., $k^*a > 2$, which gives a Ca_c of about 3.6, in good agreement with the experimental observations. This suggests the following qualitative picture for the onset of streaming: a perturbation on the interface near the stagnation equatorial line gets entrained by the converging flow to form a sheet. The surface

tension opposes the interface deformation, but its effect is weakened by the electric stresses. Indeed, the electric pressure increases significantly as the drop flattens compared to a sphere and becomes more localized near the equator (see the Supplemental Material [19]). Moreover, the shear electric stresses which drive the convergent flow strengthen as the aspect ratio increases. Both effects—stronger electric pressure and shear stress—aid the growth of the instability. In contrast to the EHD cone jetting, the sheet and subsequently formed structures (the rings and drops) are charge-free because the stagnation line is the location of zero induced charge; e.g., for a sphere, the induced charge varies as $\cos\theta$.

In a second step, the sheet pinches off at the leading edge and sheds rings with a typical radius r_c of about 20 μm; see Fig. 4. Unlike a cylindrical thread, an infinite planar thin film is capillary stable. However, the applied electric field can destabilize the film [36] because of the opposite sign of the induced charge on the film interfaces. The theory predicts a cutoff wave number $k^*h \sim 2\zeta^{1/2}$, where h is the film thickness and $\zeta = \varepsilon_{ex}E^2h/\gamma \equiv \mathrm{Ca}\,h/a$. The film thickness h can be estimated from volume conservation: the volume in a section of the thin film spanned by a wavelength $\xi = 2\pi/k^*$ after pinch-off is transferred into a ring with radius r_c; hence, $h\xi = \pi r_c^2$ (per unit edge length). Thus, we find $h \sim (r_c^4\mathrm{Ca}/a)^{1/3}$. For the $\lambda = 0.07$ drop fluid, $h \sim 10$ μm.

In a final step, the rings break into droplets via the classical capillary instability. The linear stability analysis predicts a wavelength $c(\lambda)r_c$, where $c(\lambda)$ ranges from 24.4 to 11 for viscosity ratios $\lambda = 0.001$–0.1 [37]. For $\lambda = 0.07$, we measure wavelength at 200 μm, which is in very good agreement with theory. The concentric rings break up via an out-of-phase correlation between neighboring rings: due to hydrodynamic interactions, an alternation of necking and expanding occurs along the orthogonal direction [38]; see Fig. 4(c). The capillary instability is also characterized by the formation of satellite droplets during breakup. The ratio of droplet diameter from generation to mother is a function of the viscosity ratio [39]. For $\lambda = 0.07$, the daughter-mother size ratios of the two generations visible in our experiments—indicated by the blue arrows in Fig. 4(c)—is about 0.2 and 0.1, in good agreement with the numerical predictions. One generation of a satellite cylinder is also created as a ring detaches from the edge sheet; see Fig. 4(d).

The final outcome of the streaming is the formation of thousands of microdroplets of quite uniform size; see Fig. 5. The average radius increases with the viscosity ratio as $\lambda^{1/2}$. This power-law dependency seems to originate from the slenderness of the sheet from which the cylinders are formed. According to slender body theory for a thin film of length L and thickness $h \sim r_c$, the balance of viscous shear stresses imposed by the external flow, $\mu_{ex}U/L$, and lubrication pressure in the thin film, $\lambda\mu_{ex}UL/h^2$ yields $h/L \sim \lambda^{1/2}$ [40]. Since the rings break up via capillary instability, droplet size is set by the cylinder radius and follows the same dependence on the viscosity ratio.

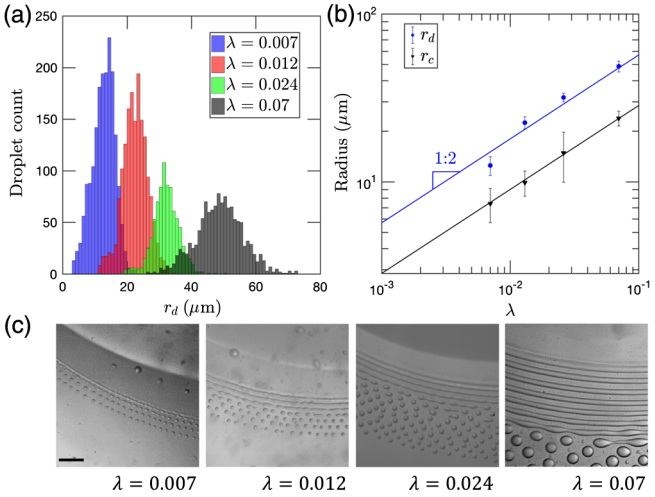

FIG. 5. (a) Droplet size distribution at varying viscosity ratios λ. The standard deviation varies between 15% and 30% of the central value. (b) The ring r_c and droplet r_d radii follow a $\sim\lambda^{1/2}$ dependence on the viscosity ratio. (c) The number of concentric rings decreases with a decreasing viscosity ratio; a ring is barely visible at $\lambda = 0.007$, and the droplets seem to originate directly from the edge sheet. The scale bar is 200 μm.

Concluding remarks.—In this Letter, we report that, upon application of a uniform dc electric field, a drop flattens and forms a sharp edge with a thin film attached to it (an edge sheet), shedding charge-free fluid rings encircling the drop. The concentric fluid rings subsequently undergo capillary instability and break up into droplets. The droplets form an initially hexagonal pattern in the equatorial plane of the mother drop. The streaming occurs only for low viscosity drops, with a viscosity ratio smaller than 0.1 and field strengths corresponding to $\mathrm{Ca} \geq 4$.

While the detailed mechanism of the streaming is yet to be quantified, the phenomenon is reasonably explained by the interfacial instability of the stagnation line of a convergent flow [6]. The flow is driven by electric shear stresses on the drop interface and converges at the equator. A perturbation of the compressed interface grows and a fluid sheet is drawn from the equator, which is the stagnation line. The growth of the interface deformation into an edge-sheet structure is aided by he normal electric stresses which overcome the surface tension.

EHD equatorial streaming allows the production of large number of microdroplets in a relatively short time. The final droplet size can be tuned by changing the viscosity ratio. This study suggests methods of microdroplet production in a bulk environment, "electroemulsification," with potential applications in industrial processes.

We hope our experimental observations will inspire further work on this phenomenon. Numerical simulations are needed to explain the effects of viscosity ratio and field strength in the selection of the "streaming" versus the "dimpling" mode of drop destabilization. The nature of the instability suggests that equatorial streaming from a drop

can be obtained in the absence of an electric field—for example, a surfactant-covered drop in axisymmetric compressional flow.

This research was supported by NSF Grants No. CBET-1437545 and No. CMMI-1538703.

*Present address: Engineering Sciences and Applied Mathematics, Northwestern University, Evanston, IL 60208, USA.

[1] J. F. de la Mora, Annu. Rev. Fluid Mech. **39**, 217 (2007).
[2] R. T. Collins, K. Sambath, M. T. Harris, and O. A. Basaran, Proc. Natl. Acad. Sci. U.S.A. **110**, 4905 (2013).
[3] R. T. Collins, J. J. Jones, M. T. Harris, and O. A. Basaran, Nat. Phys. **4**, 149 (2008).
[4] E. O. Elele, Y. Shen, D. R. Pettit, and B. Khusid, Phys. Rev. Lett. **114**, 054501 (2015).
[5] O. A. Basaran, H. Gao, and P. P. Bhat, Annu. Rev. Fluid Mech. **45**, 85 (2013).
[6] Y.-H. Tseng and A. Prosperetti, J. Fluid Mech. **776**, 5 (2015).
[7] R. Suryo and O. A. Basaran, Phys. Fluids **18**, 082102 (2006).
[8] E. Castro-Hernandez, F. Campo-Cortes, and J. Manuel Gordillo, J. Fluid Mech. **698**, 423 (2012).
[9] S. L. Anna, Annu. Rev. Fluid Mech. **48**, 285 (2016).
[10] J. Eggers, Phys. Rev. Lett. **86**, 4290 (2001).
[11] G. I. Taylor, Proc. R. Soc. A **291**, 159 (1966).
[12] J. R. Melcher and G. I. Taylor, Annu. Rev. Fluid Mech. **1**, 111 (1969).
[13] E. Lac and G. M. Homsy, J. Fluid Mech. **590**, 239 (2007).
[14] O. Ghazian, K. Adamiak, G. S. P. Castle, and Y. Higashiyama, Colloids Surf. A **441**, 346 (2014).
[15] M. Zabarankin, I. Smagin, O. M. Lavrenteva, and A. Nir, J. Fluid Mech. **720**, 169 (2013).
[16] S. Torza, R. G. Cox, and S. G. Mason, Phil. Trans. R. Soc. A **269**, 295 (1971).
[17] A. S. Mohamed, J. M. Lopez-Herrera, M. A. Herrada, L. B. Modesto-Lopez, and A. M. Ganan-Calvo, Langmuir **32**, 6815 (2016).
[18] P. F. Salipante and P. M. Vlahovska, Phys. Fluids **22**, 112110 (2010).
[19] See Supplemental Material at http://link.aps.org/supplemental/10.1103/PhysRevLett.119.034501, which includes Refs. [20–23], for additional details about the experimental system and the theoretical models.
[20] H. Nganguia, Y. N. Young, P. M. Vlahovska, J. Blawzdziewcz, J. Zhang, and H. Lin, Phys. Fluids **25**, 092106 (2013).
[21] H. Nganguia and Y. N. Young, Phys. Rev. E **88**, 052718 (2013).
[22] P. G. Drazin, *Introduction to Hydrodynamic Stability* (Cambridge University Press, Cambridge, England, 2002).
[23] P. M. Vlahovska, J. Fluid Mech. **670**, 481 (2011).
[24] P. M. Vlahovska, Phys. Rev. Fluids **1**, 060504 (2016).
[25] E. Yariv and I. Frankel, J. Fluid Mech. **788**, R2 (2016).
[26] P. F. Salipante and P. M. Vlahovska, Phys. Rev. E **88**, 043003 (2013).
[27] H. He, P. F. Salipante, and P. M. Vlahovska, Phys. Fluids **25**, 032106 (2013).
[28] T. B. Jones, IEEE Trans. Ind. Appl. **IA-20**, 845 (1984).
[29] E. Pairam and A. Fernández-Nieves, Phys. Rev. Lett. **102**, 234501 (2009).
[30] G. I. Taylor, Proc. R. Soc. A **253**, 313 (1959).
[31] C. Clanet, Annu. Rev. Fluid Mech. **39**, 469 (2007).
[32] J. Eggers and E. Villermaux, Rep. Prog. Phys. **71**, 036601 (2008).
[33] L. V. Zhang, P. Brunet, J. Eggers, and R. D. Deegan, Phys. Fluids **22**, 122105 (2010).
[34] A. M. Ganan-Calvo and J. M. Montanero, Phys. Rev. E **79**, 066305 (2009).
[35] A. M. Ganan-Calvo, J. M. Lopez-Herrera, N. Rebollo-Munoz, and J. M. Montanero, Sci. Rep. **6**, 32357 (2016).
[36] D. H. Michael and M. E. O'Neill, J. Fluid Mech. **41**, 571 (1970).
[37] S. Tomotika, Proc. R. Soc. A **150**, 322 (1935).
[38] Z. Zhang, G. C. Hilton, R. Yang, and Y. Ding, Soft Matter **11**, 7264 (2015).
[39] M. Tjahjadi, H. A. Stone, and J. M. Ottino, J. Fluid Mech. **243**, 297 (1992).
[40] H. A. Stone, Annu. Rev. Fluid Mech. **26**, 65 (1994).